Supporting Information for

Surface Dynamics and Ligand-Core Interactions of Quantum Sized Photoluminescent Gold Nanoclusters

Yiyang Lin,[1,†] Patrick Charchar,[2,†] Andrew J. Christofferson,[2] Michael R. Thomas,[1] Nevena Todorova,[2] Manuel M. Mazo,[1] Qu Chen,[1] James Doutch,[3] Robert Richardson,[4] Irene Yarovsky,[2,*] & Molly M. Stevens[1,*]

[1]Department of Materials and Department of Bioengineering, Institute of Biomedical Engineering, Imperial College London, Exhibition Road, London SW7 2AZ, United Kingdom

[2]School of Engineering, RMIT University, Melbourne Victoria 3001, Australia

[3]ISIS Neutron and Muon Source, STFC, Harwell Science and Innovation Campus, Didcot, Oxfordshire OX11 0QX

[4]H. H. Wills Physics Laboratory, University of Bristol, Bristol BS8 1TL, United Kingdom

*Phone: +61 (3) 9925 2571. Fax: +61 (3) 9925 5290. Email: irene.yarovsky@rmit.edu.au

*Phone: +44 (0)207 594 6804 1. Fax: +44 (0)207 594 6757. Email: m.stevens@imperial.ac.uk

[†]These authors contributed equally to this work.

Methods

Reagents and materials. All Fmoc-protected amino acids, Rink Amide resin, and *O*-benzotriazole-*N*, *N*, *N*', *N*'-tetramethyluronium-hexafluoro-phosphate (HBTU) were purchased from Anaspec. Inc. All the other reagents were used as received.

Solid phase peptide synthesis. Peptides were synthesized using standard FMOC solid state synthesis using Rink amide resin. Protected amino acids were added to the growing peptide chain with the activating reagent HBTU. Upon the addition of the N-terminal amino acid, the FMOC group was removed under standard 20% piperidine in DMF deprotection conditions. The peptides were cleaved from resin by 20 mL of trifluoroacetic acid/triisopropylsilane/water (95:2.5:2.5, v/v/v) containing dithiothreitol. The crude peptide was precipitated by cold ether several times and applied to reverse phase high performance liquid chromatography (HPLC, Shimadzu) to purify the target peptide. The Phenomenex C18 Gemini NX column was 150 x 21.2 mm and had a 5 μm particle size and 110 Å pore size. Matrix-assisted laser desorption spectroscopy (MALDI; Waters) was used to confirm the expected *m/z* ratio and α-Cyano-4-hydroxycinnamic acid was used as the MALDI matrix substance.

Synthesis of photoluminescent AuNCs. To synthesize peptide-protected AuNCs, 0.5 mM $HAuCl_4$ were added into an aqueous solution of 2.0 mM peptide followed by vortexing for 10 sec. After 30 min, freshly

prepared sodium cyanoborohydride was introduced to reduce gold ions at room temperature. The solution was stored in the dark overnight before further characterization.

Characterization of AuNCs. UV-Vis absorbance was measured on Shimadzu (UV-1800) UV-visible spectrometer with a scanning speed of 20 nm/sec. Fluorescence excitation and emission measurements were performed on Fluorolog®-3 spectrofluorometer. Quantum yield of AuNCs was obtained using the comparative method with Rhodamine 6G ethanolic solution (QY = 95 %, λ_{ex} = 488 nm) as a standard fluorophore. XPS spectra were obtained on a Thermo Fisher K-Alpha spectrophotometer utilizing a monochromatic Al-Ka X-ray source (energy = 1486.71 eV). TEM imaging was performed on a JEOL 2100F with an acceleration voltage of 200 kV and elemental compositional analysis of gold clusters was determined by energy-dispersive X-ray spectroscopy (EDS). The time-resolved fluorescence measurements were acquired with a Horiba Deltaflex system, using a 404 nm diode laser with a pulse duration of <100 ps as the light excitation source (λ = 700 nm). The IRF was collected at the excitation wavelength using a diluted Ludox© solution in water. Polyacrylamide gel electrophoresis (PAGE) experiment was performed by using a slab gel electrophoresis unit following the reported method.[1,2] The separating and stacking gels were prepared by acrylamide monomers with the total contents of 25 and 3 wt % (acrylamide/bis-acrylamide, 19:1), respectively. The eluting buffer contains 25 mM tris(hydroxymethylamine) and 192 mM glycine. The sample solution (20 μL) was loaded onto the stacking gel and eluted at a constant voltage mode (200 V).

Cell culture. All products from Life Technologies (UK) unless otherwise stated. HeLa cells were obtained from DSMZ (Brunswick, Germany) and maintained under standard mammalian cell culture conditions in DMEM supplemented with fetal bovine serum (10%, v:v) and penicillin-streptomycin (1%, v:v). For the particle uptake experiments, cells were plated at 10^5 cells per well in 8 well chamber slides (Ibidi, UK). On the next day, the particle solution in sterile PBS was added to each well in serial dilutions, supplemented with an equal volume of culture medium and incubated for 24 hours, after which the samples were fixed in paraformaldehyde (4%, w:v) for 15 minutes and washed extensively in PBS.

Cell staining and confocal imaging. To visualize the cell membrane and nucleus, the samples were stained with WGA-488 and DAPI for 15 min following manufacturer´s instructions. After washing in PBS, images were taken using a Leica SP5 MP/FLIM inverted confocal microscope. Laser reflection and infrared emission were both used to localize the particles.

Computational simulation details. The AuNC structure used in the molecular dynamics (MD) simulations contains 25 gold atoms and a morphology consistent with that of highly stable $Au_{25}(SR)_{18}$ clusters, which can conceptually be divided into an icosahedral Au_{13} core protected by six –[SR–(Au-SR)$_2$]– "staple" motifs.[3] The peptide-coated AuNCs modeled (indicated by asterisks in Table S1) were constructed by attaching, *via* the N-terminal cysteine, 18 extended peptide ligands equidistantly onto the X-ray crystal structure[3] of $Au_{25}(SR)_{18}$ (Fig. 1b). All peptides have been NH_2 capped on the C-terminus and N-terminated with either a NH_3^+ moiety or a CH_3CO acetyl group (denoted by an "Ac-" prefix). In total, 14 different $Au_{25}(SP)_{18}$ (P = peptide) simulation models were constructed with the following peptide sequences: CGGGDD as a control; CVGGDD, CHGGDD, CYGGDD, CGYGDD, CHYGDD, CYHGDD, CYYGDD, and CVVGDD to explore hydrophobicity and individual amino acid location; Ac-CGGGDD, Ac-CHGGDD, Ac-CHYGDD and Ac-

CYHGDD to study N-terminal acetyl capping; as well as an additional positively charged peptide with arginine residues, CYYGRR, to investigate a cellular internalizing sequence. The chosen $Au_{25}(SP)_{18}$ models represent diverse and distinct experimental systems which display a distribution of PL intensities.

Explicit solvent MD simulations were conducted using the GROMACS 4.6.5 software.[4] Peptide interatomic interactions were modelled using the all-atom AMBER99SB-ILDN force field (FF),[5] with CYX parameters used for charge neutral (unprotonated) cysteine residues. The TIP3P model was used for water.[6] Bonded parameters and Lennard-Jones potentials between Au and peptide atoms (S, C, and H) were adopted from a FF parameterized for similar monolayer-protected AuNCs assuming no explicit partial charges on gold atoms.[7] Additional parameters for the Au-S-C-C dihedral were obtained from a quantum mechanics dihedral scan at the B3LYP/6-31G* level (with the LanL2DZ basis set for Au) in Gaussian09.[8] For non-bonded interactions, long-range electrostatics were evaluated using the Particle Mesh Ewald (PME) method with a real space cutoff of 10 Å and a 1.2 Å fast Fourier transform (FFT) grid spacing, while van der Waals interactions were truncated at 10 Å. To preserve the core crystal structure[3] of $Au_{25}(SP)_{18}$ during MD, distance restraints[9] of 1000 kJ/mol/nm^2 were applied between Au-Au atoms. Each $Au_{25}(SP)_{18}$ was placed in a periodic cubic box of side length ~8.4 nm, solvated with ~19000 water molecules (water density of ~1 g/cm^3) and Na^+ or Cl^- counter ions were added to ensure a neutral simulation cell. Energy minimization was carried out using the steepest descent algorithm to remove any steric clashes and 1 ns of position restrained MD was performed using the Berendsen[10] thermostat and barostat to equilibrate the solvent around the AuNCs at 300 K temperature and 1 atm pressure. Position restraints were then removed and 100 ns of NPT (constant pressure and temperature ensemble) MD was performed with the Nosé-Hoover thermostat[11] and Parrinello-Rahman barostat[12] to maintain temperature and pressure at 300 K and 1 atm. The LINCS algorithm[13] was applied to constrain all bonds to their equilibrium lengths, which enabled a time-step of 2 fs to be used for each simulation, and frames were outputted to a trajectory file every 2 ps. To enhance conformational sampling, each system was simulated ten times starting from different initial atomic velocities, resulting in a total of 1 μs of data for each $Au_{25}(SP)_{18}$. Statistical analysis and visualization of the data was performed using the GROMACS 4.6.5 suite analysis tools[4] and the VMD 1.9.2 package.[14] The properties and structures presented are ensemble averaged over the 10 independent trajectories for each $Au_{25}(SP)_{18}$ system and, unless stated otherwise, analysis has been performed on the thermally equilibrated stage of the simulations covering the final 20 ns of each trajectory (200 ns of production data per system), as verified by monitoring energy trends, convergence of R_g and root-mean-square deviations. Hydrodynamic diameter (D_h) estimates are obtained for 2×10^4 configurations per system (1 frame every 10 ps) using the path-integration program ZENO[15] with 1.5×10^5 random paths at each configuration to achieve low uncertainty in D_h.

Quantum mechanics (QM) calculations were performed in a manner similar to the approach of Fihey et al.[16] Initial geometries of the $Au_{25}S_{18}$Cys AuNCs with acetyl, protonated amine, and deprotonated amine N-termini were taken from equilibrated MD simulation snapshots. A geometry optimization of the cysteine ligands with N-methylamine C-termini was performed using the DMoL^3 program[17] with the PBE DFT exchange correlation functional[18] and double-numeric polarized (DNP) basis set[19] with all electron relativistic core treatment. Solvent effects were treated using the conductor-like screening model

(COSMO).[20] Electrostatic potential (ESP) atomic partial charge calculations of the optimized structures were performed using Gaussian09,[8] with the PBE DFT functional and the relativistic double-ζ LanL2DZ basis set and effective core potential (ECP) for Au atoms, and the 6-311G(d,p) basis set for other atoms. Solvent effects were treated using the Polarizable Continuum Model (PCM).[21]

Table S1. Engineered sequences used to prepare peptide-protected AuNCs.

CXXGDD	***Ac-CXXGDD***	***Other***
CGGGDD*	Ac-CGGGDD*	CDGGGD
CSGGDD	Ac-CHGGDD*	DGYCGD
CVGGDD*	Ac-CHYGDD*	CYYGRR*
CTGGDD	Ac-CYHGDD*	
CHGGDD*		
CKGGDD		
CFGGDD		
CQGGDD		
CNGGDD		
CYGGDD*		
CGYGDD*		
CVVGDD*		
CHYGDD*		
CYHGDD*		
CYYGDD*		
CFFGDD		

*$Au_{25}(SP)_{18}$ (P = peptide) structures also investigated with molecular modelling.

Figure S1. Polyacrylamide gel electrophoresis (PAGE) result for the CHYGDD-protected AuNCs.

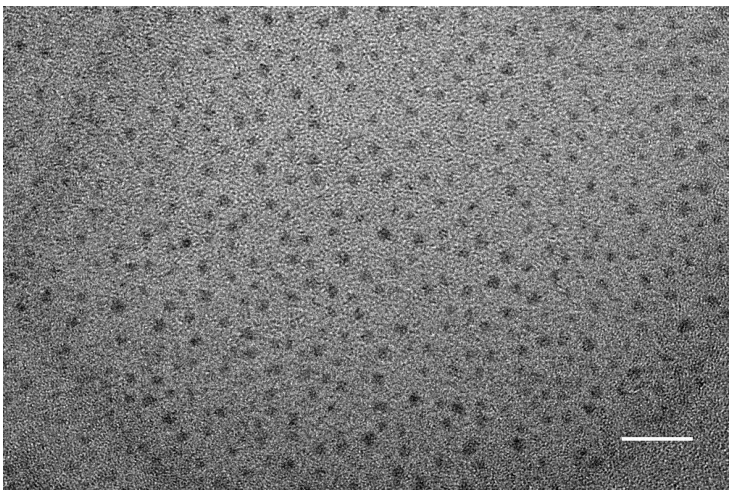

Figure S2. Representative transmission electron microscopy (TEM) image of CHYGDD-protected AuNCs showing the uniform, ultra-small nanoparticles. Scale bar: 10 nm.

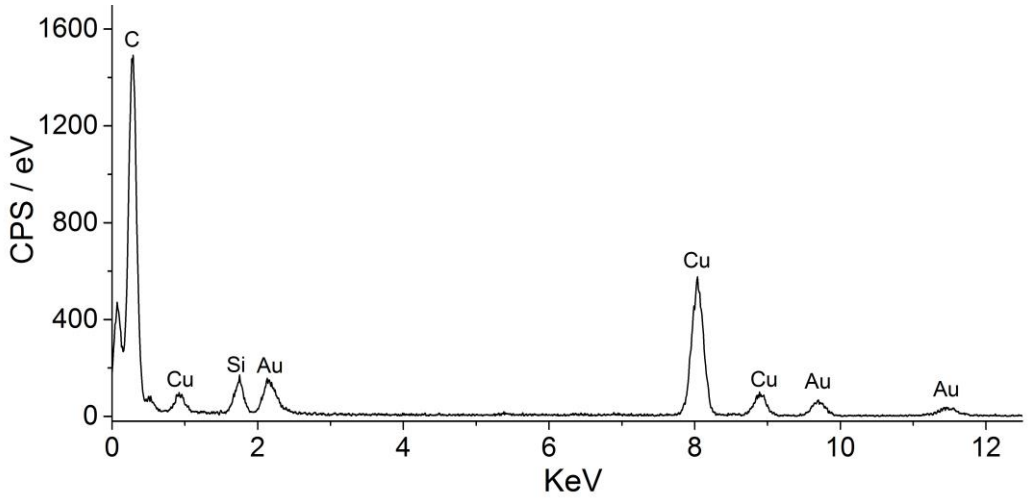

Figure S3. Energy-dispersive X-ray spectroscopy (EDS) of CHYGDD-protected AuNCs showing the existence of Au elements in the nanoclusters.

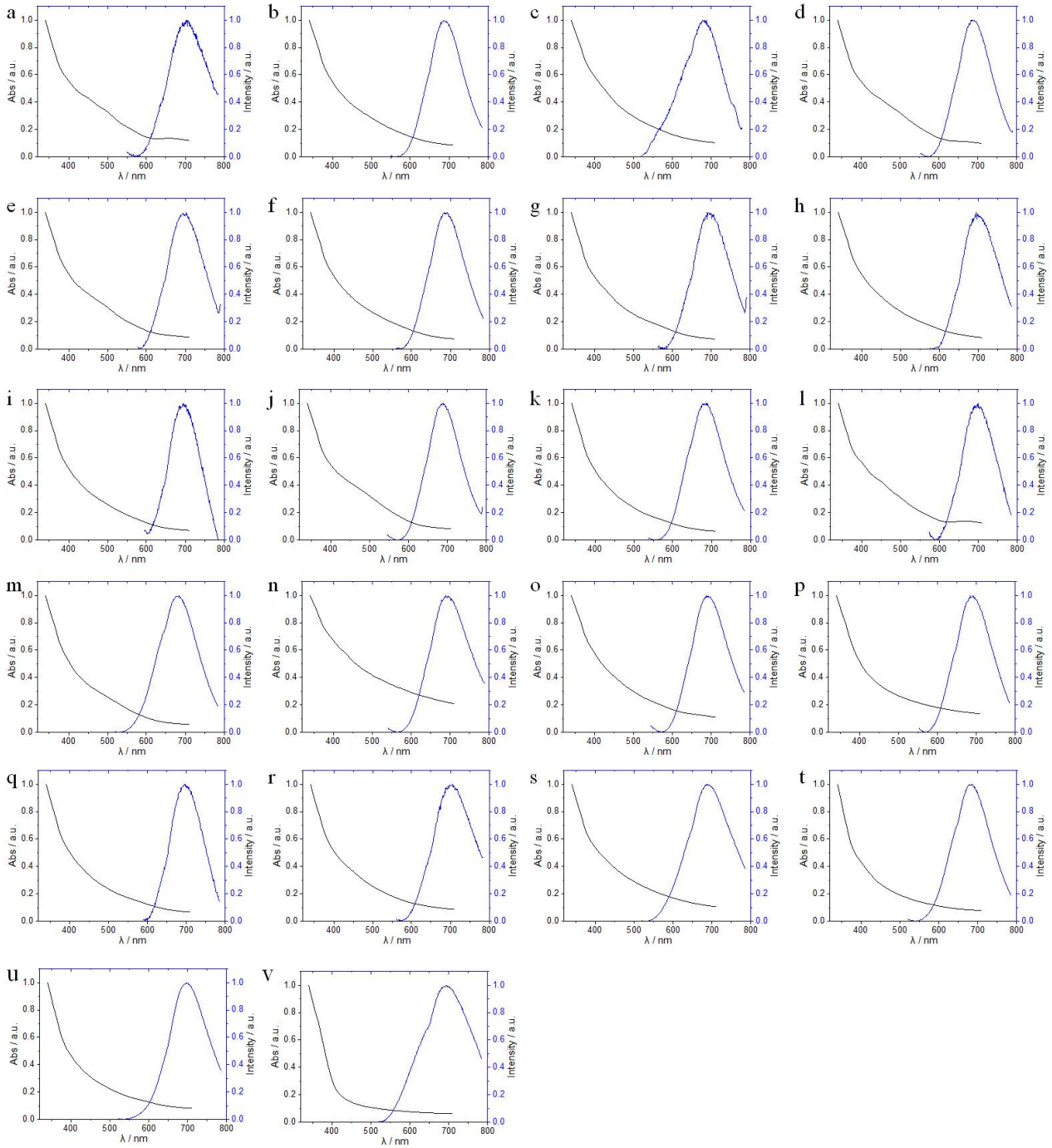

Figure S4. UV-vis absorbance and fluorescence emission spectra of Au clusters protected by different peptide molecules: (a) CGGGDD, (b) CFGGDD, (c) CHGGDD, (d) CYGGDD, (e) CSGGDD, (f) CVGGDD, (g) CDGGGD, (h) CKGGDD, (i) CTGGDD, (j) CGYGDD, (k) CVVGDD, (l) CNGGDD, (m) CYYGDD, (n) CHYGDD, (o) CYHGDD, (p) CFFGDD, (q) CQGGDD, (r) Ac-CGGGDD, (s) Ac-CHGGDD, (t) Ac-CHYGDD, (u) Ac-CYHGDD, and (v) DGYCGD. The excitation wavelength was 400 nm.

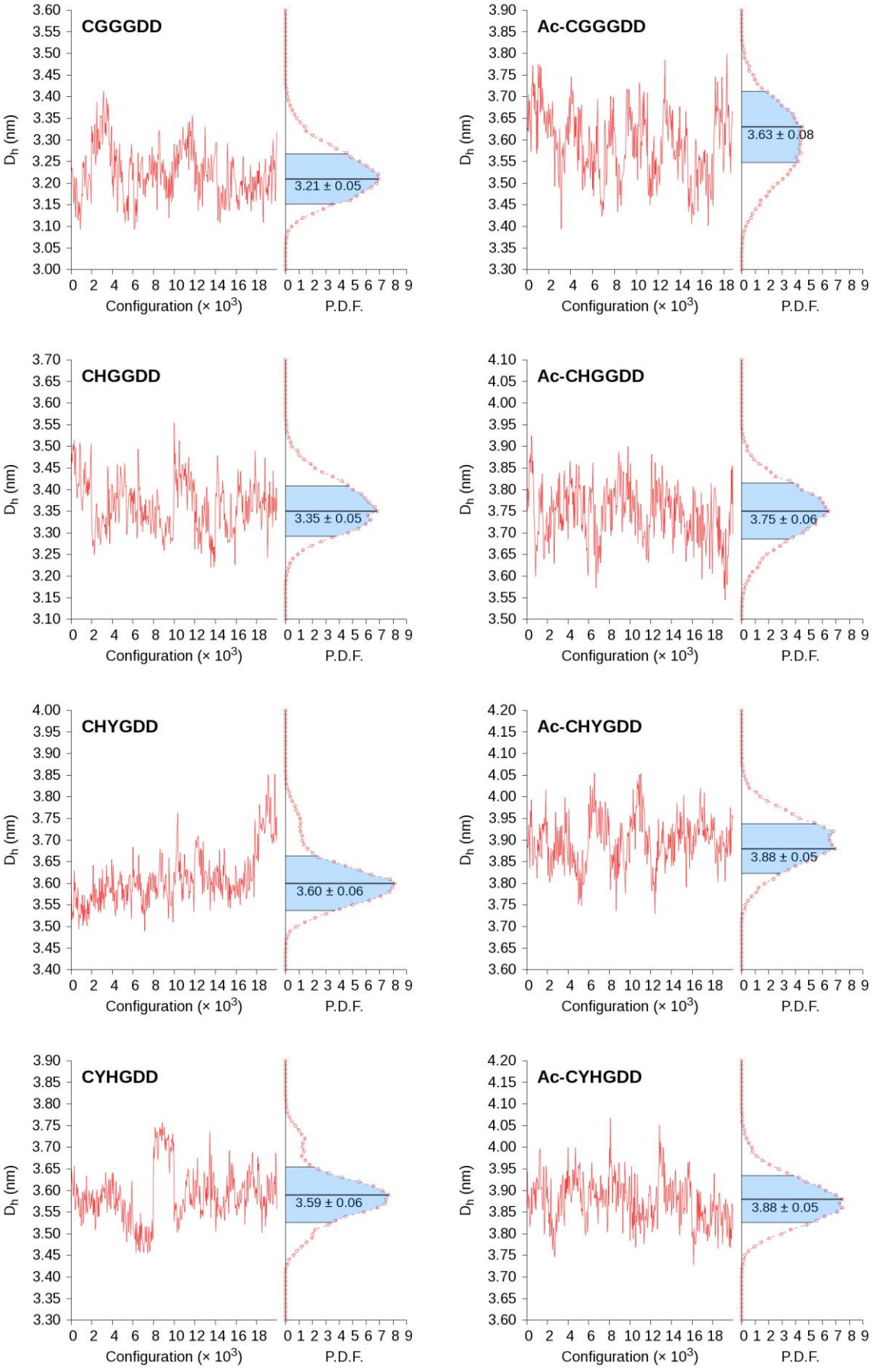
CGGGDD
3.21 ± 0.05
Ac-CGGGDD
3.63 ± 0.08
CHGGDD
3.35 ± 0.05
Ac-CHGGDD
3.75 ± 0.06
CHYGDD
3.60 ± 0.06
Ac-CHYGDD
3.88 ± 0.05
CYHGDD
3.59 ± 0.06
Ac-CYHGDD
3.88 ± 0.05
Dh (nm)
Configuration (× 10^3)
P.D.F.

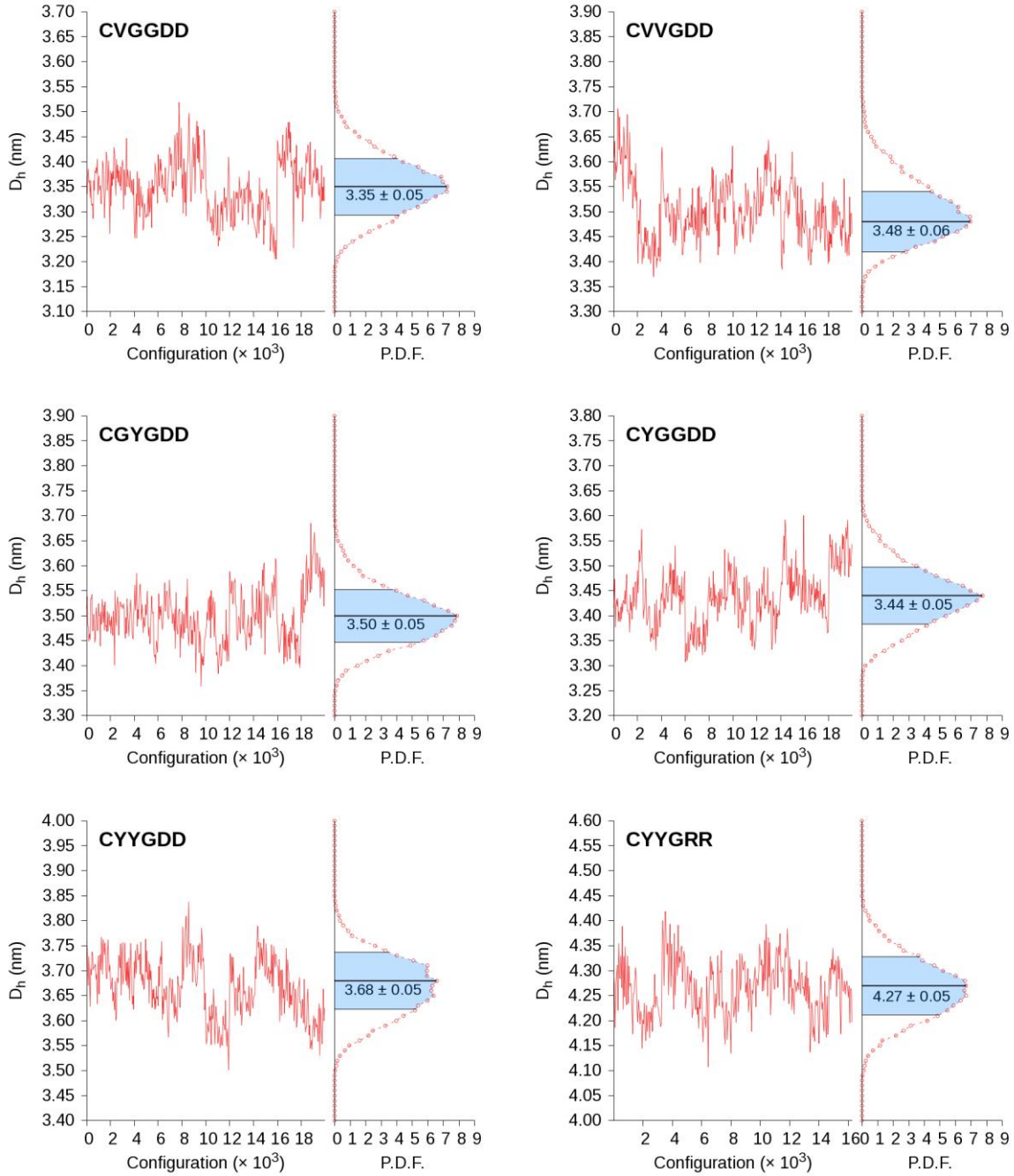

Figure S5. Left panels: Hydrodynamic diameter (D_h) computed for 2×10^4 configurations using the ZENO[15] path-integration program. It should be noted that configurations within consecutive blocks of 2×10^3 are correlated since they are taken from independent equilibrated trajectories and only every 50^{th} data point is plotted for clarity. **Right panels**: Probability density function (P.D.F.) of the ensemble shown with the modal D_h and one standard deviation (shaded region).

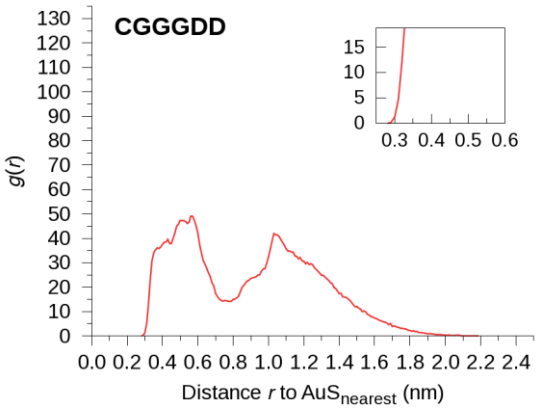
CGGGDD
g(r)
Distance r to AuS$_{nearest}$ (nm)

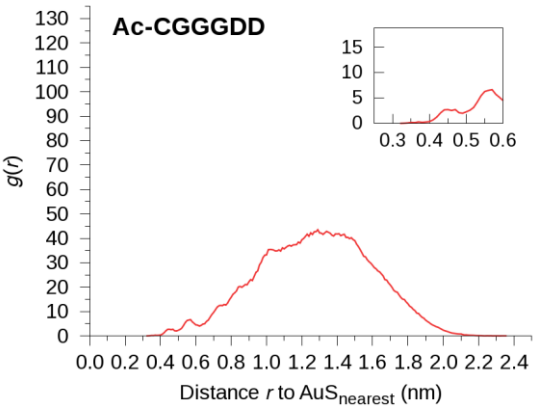
Ac-CGGGDD
g(r)
Distance r to AuS$_{nearest}$ (nm)

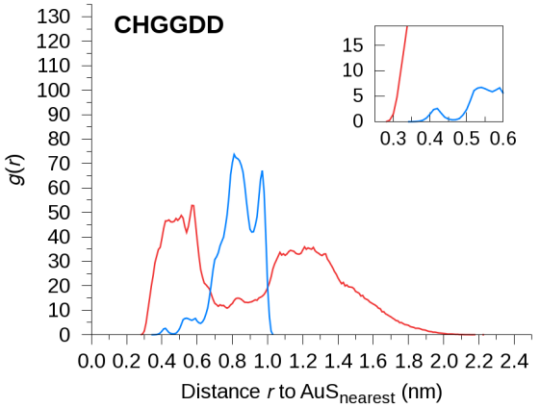
CHGGDD
g(r)
Distance r to AuS$_{nearest}$ (nm)

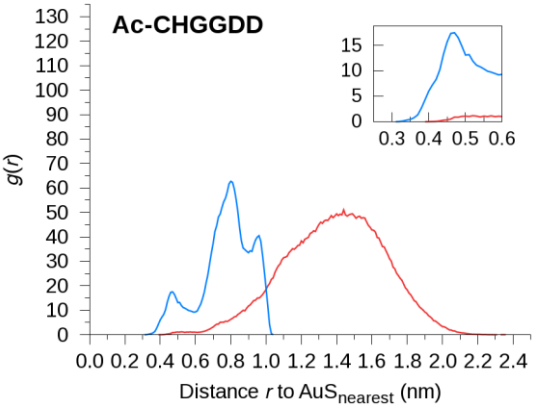
Ac-CHGGDD
g(r)
Distance r to AuS$_{nearest}$ (nm)

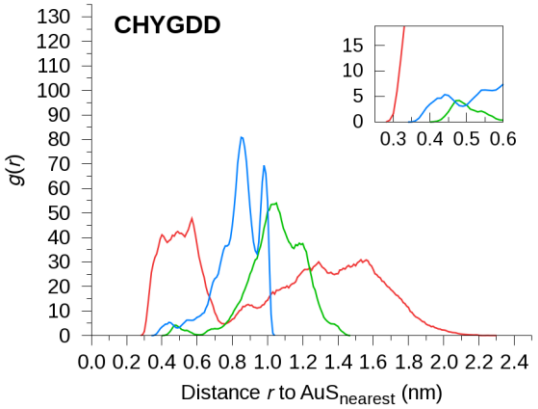
CHYGDD
g(r)
Distance r to AuS$_{nearest}$ (nm)

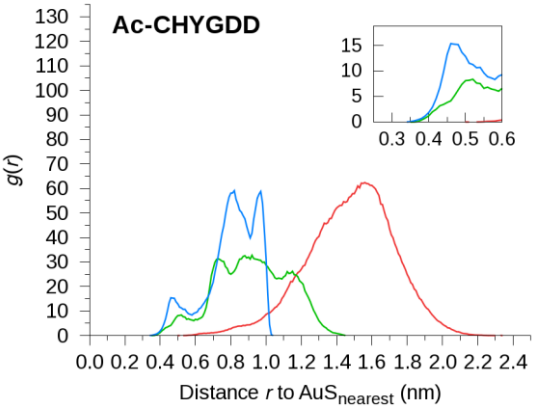
Ac-CHYGDD
g(r)
Distance r to AuS$_{nearest}$ (nm)

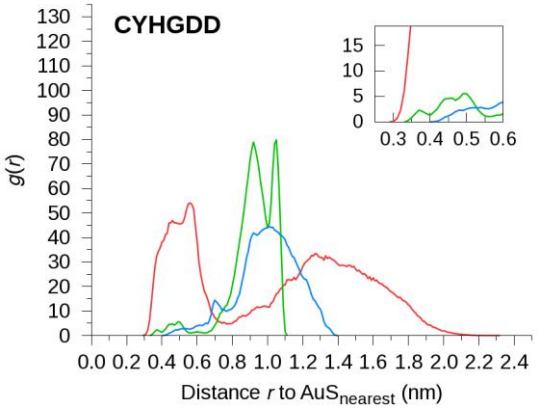
CYHGDD
g(r)
Distance r to AuS$_{nearest}$ (nm)

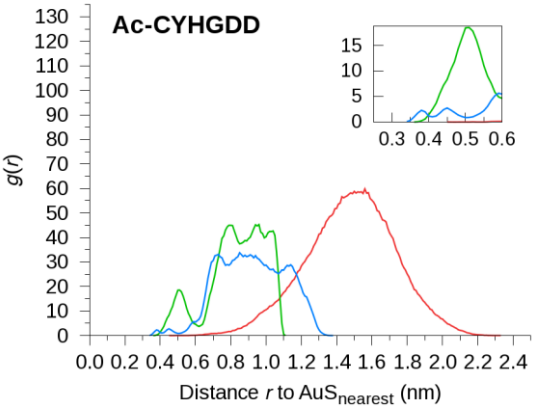
Ac-CYHGDD
g(r)
Distance r to AuS$_{nearest}$ (nm)

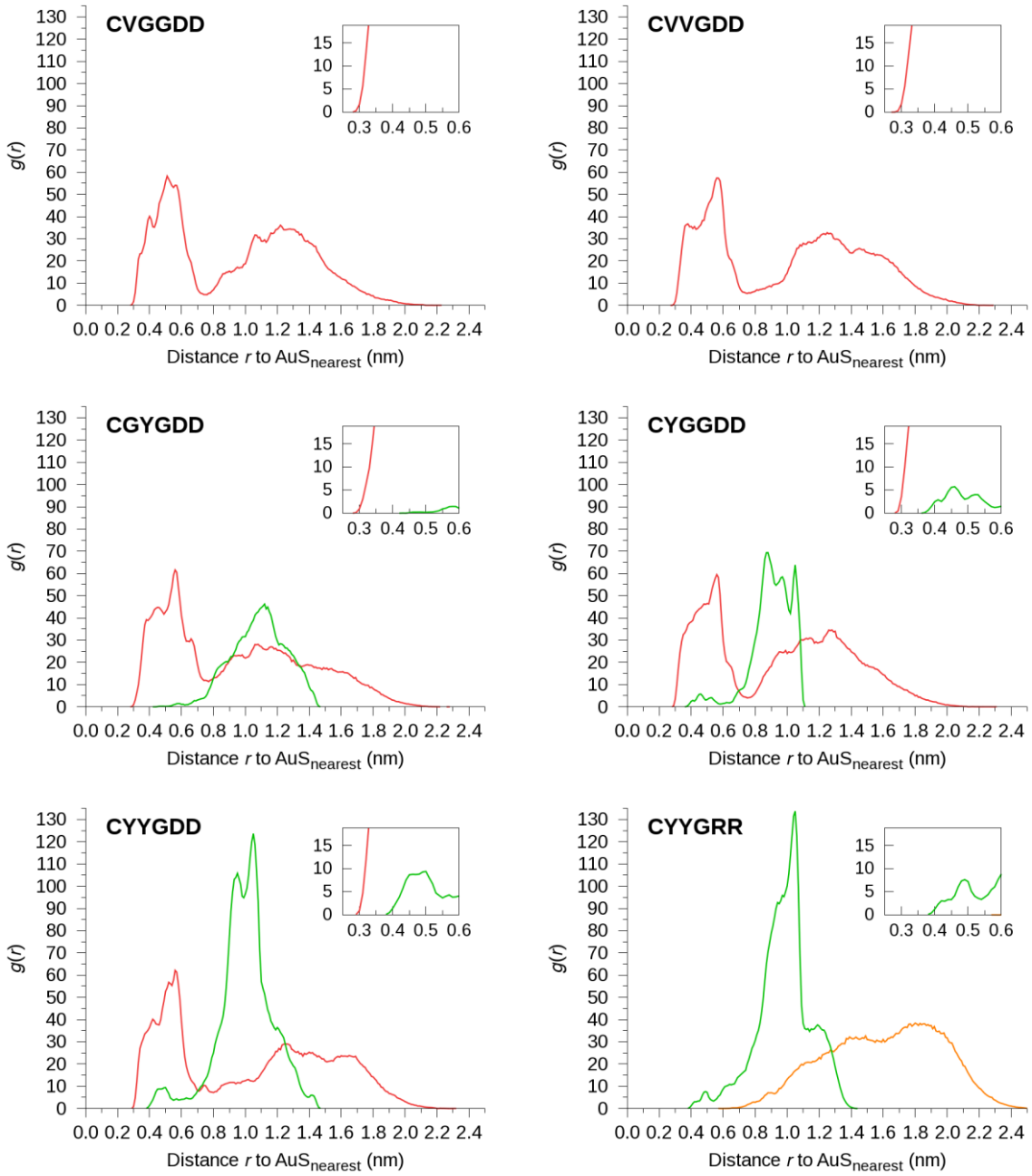

Figure S6. Pairwise distribution functions, $g(r)$, for each sequence showing the minimum distances from ASP (red), TYR (green), HIS (blue), and ARG (orange) residues to the closest $Au_{25}S_{18}$ atom. The insets in each plot show a zoomed in region to better illustrate the probability of residues being within close proximity to the gold core. The distributions of *minimum* distances are measured between the centers-of-mass of side-chain heavy-atoms (TYR: phenol, ASP: carboxyl oxygen, and HIS: imidazole) relative to the nearest gold or sulfur atom ($AuS_{nearest}$).

Table S2. Average number of residues (ASP, TYR, HIS, ARG) within 0.5 nm of $Au_{25}S_{18}$.*

System	ASP		TYR		HIS	
CGGGDD	6.74	(0.35 nm)		-		-
CVGGDD	6.65	(0.36 nm)		-		-
CVVGDD	6.26	(0.36 nm)		-		-
CHGGDD	6.85	(0.36 nm)		-	0.15	(0.65 nm)
CHYGDD	6.58	(0.36 nm)	0.21	(0.80 nm)	0.49	(0.59 nm)
CYHGDD	6.31	(0.37 nm)	0.50	(0.72 nm)	0.12	(0.70 nm)
CGYGDD	6.52	(0.37 nm)	0.01	(0.81 nm)		-
CYGGDD	7.14	(0.35 nm)	0.44	(0.70 nm)		-
CYYGDD	6.57	(0.36 nm)	0.71	(0.55 nm)		-
Ac-CGGGDD	0.22	(0.66 nm)		-		-
Ac-CHGGDD	0.05	(0.83 nm)		-	1.44	(0.47 nm)
Ac-CHYGDD	0.00	(0.97 nm)	0.44	(0.58 nm)	1.08	(0.50 nm)
Ac-CYHGDD	0.00	(0.98 nm)	0.91	(0.51 nm)	0.26	(0.65 nm)
System	**ARG**		**TYR**		**-**	
CYYGRR	0.00	(0.94 nm)	0.45	(0.61 nm)		-

*Values in parentheses are distances between $Au_{25}S_{18}$ atoms and the nearest (integer) residue.

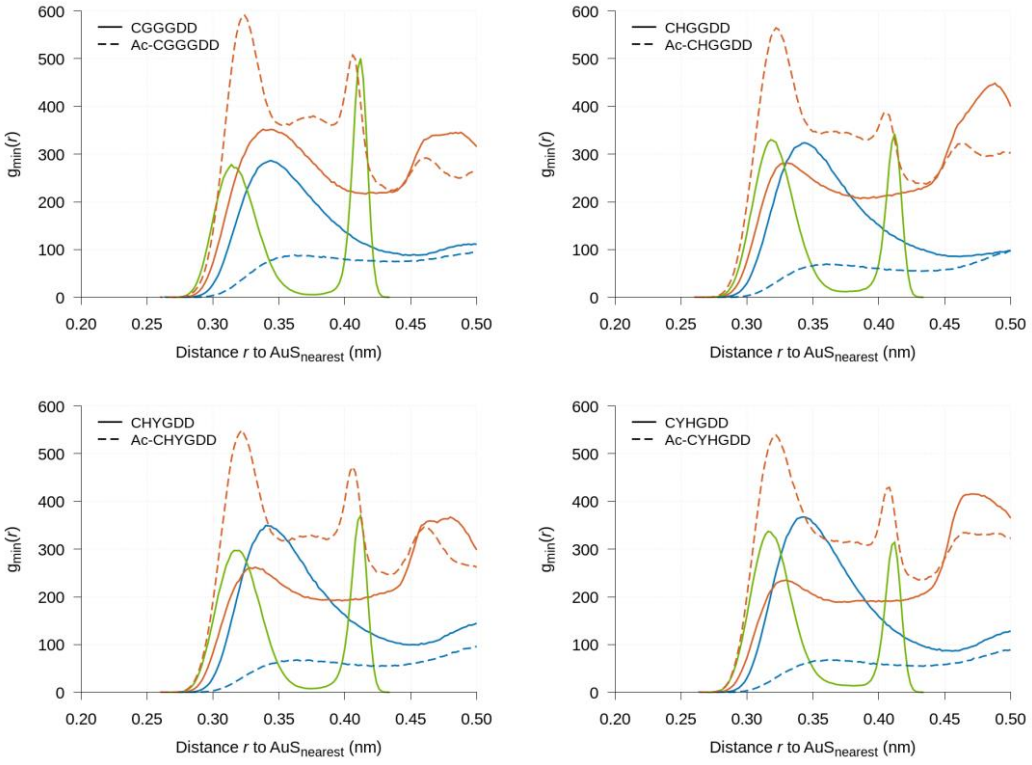

Figure S7. Pairwise distribution functions, $g(r)$, of electron-rich (red), electron-deficient (green) and water molecules (blue) relative to the closest $Au_{25}S_{18}$ atom ($AuS_{nearest}$). Distributions for atoms in uncapped systems are shown as solid lines while those for the acetyl-capped are dashed. Electron-donating groups include backbone/acetyl amine nitrogens, backbone/acetyl carbonyl oxygens, tyrosine phenol oxygen, aspartate carboxyl oxygens, histidine deprotonated imidazole nitrogen. Electron-withdrawing groups are cysteine protonated amine nitrogen. Water molecules are taken as their oxygen atom location.

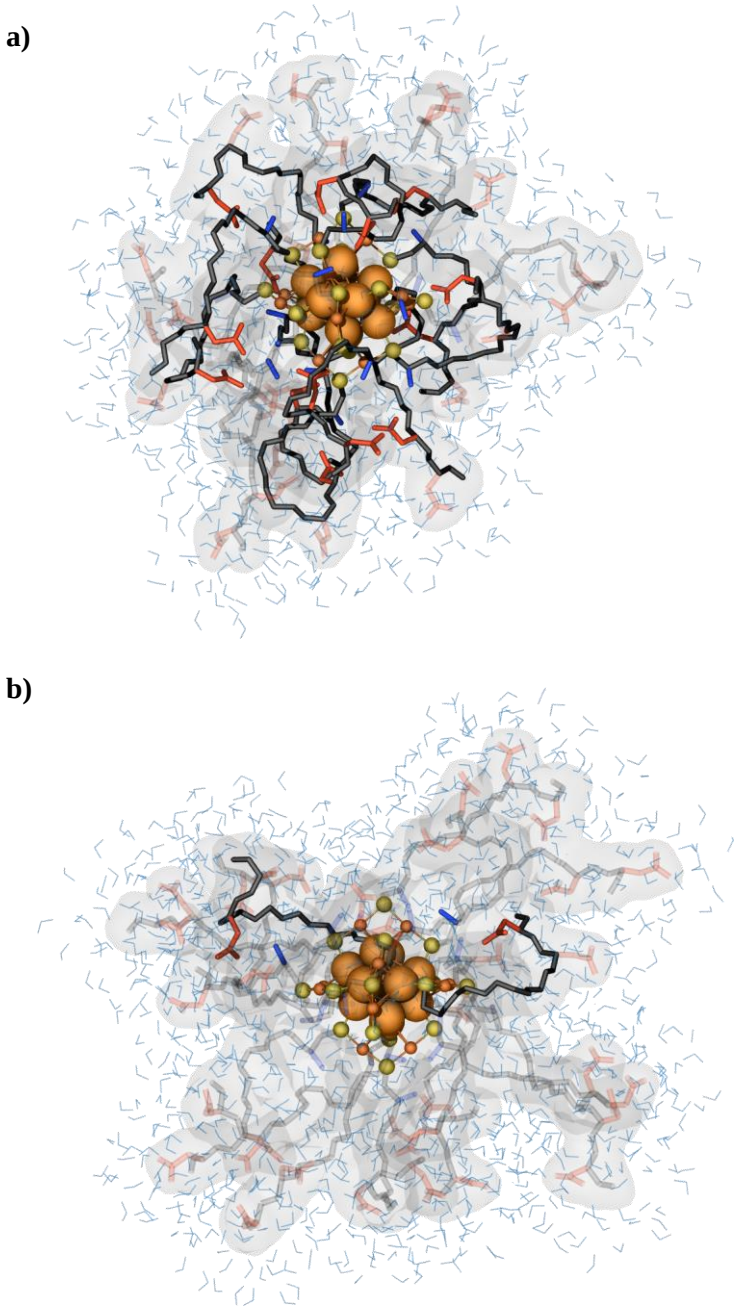

Figure S8. Representative structures of (a) CGGGDD and (b) Ac-CGGGDD showing how the presence of N-terminal NH_3^+ groups encourage more compact peptide structures due to the electrostatic attraction with C-terminal COO^- groups. Peptide backbones are shown as black lines, gold atoms are orange, sulfur atoms are yellow, ASP carbonyl oxygen atoms and CYS amine nitrogen atoms are displayed in red and dark blue, respectively. Bulk water molecules and counter ions are not shown for clarity. Peptides with COO^- groups not within close proximity of $Au_{25}S_{18}$ are drawn transparently.

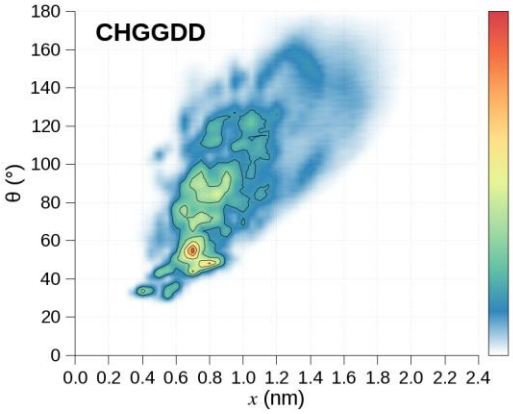
CHGGDD
θ (°)
x (nm)

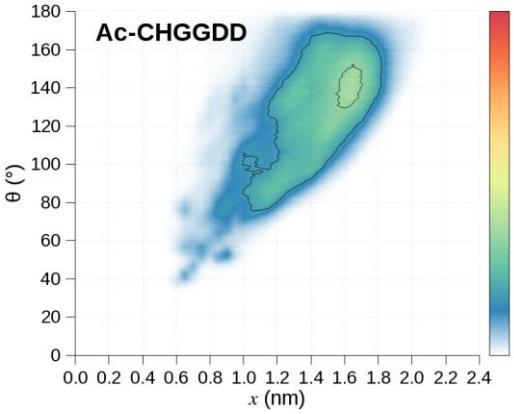
Ac-CHGGDD
θ (°)
x (nm)

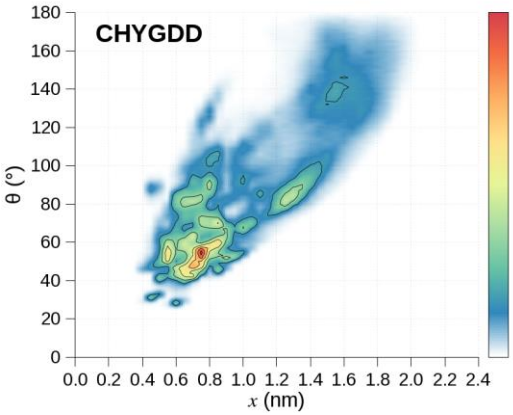
CHYGDD
θ (°)
x (nm)

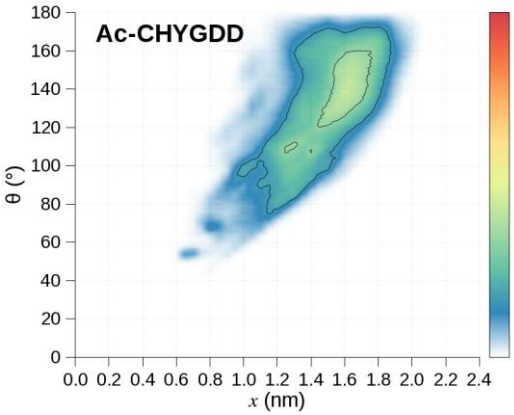
Ac-CHYGDD
θ (°)
x (nm)

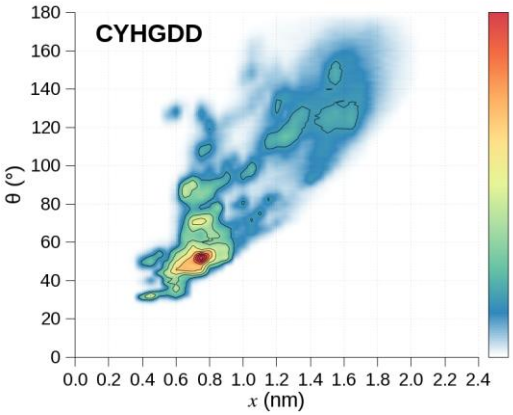
CYHGDD
θ (°)
x (nm)

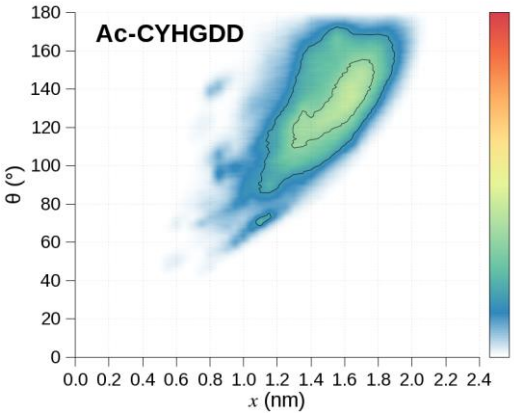
Ac-CYHGDD
θ (°)
x (nm)

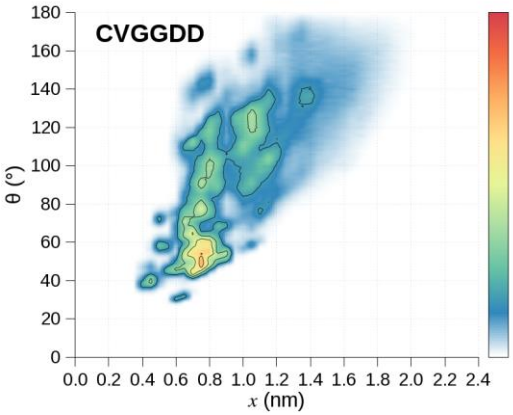
CVGGDD
θ (°)
x (nm)

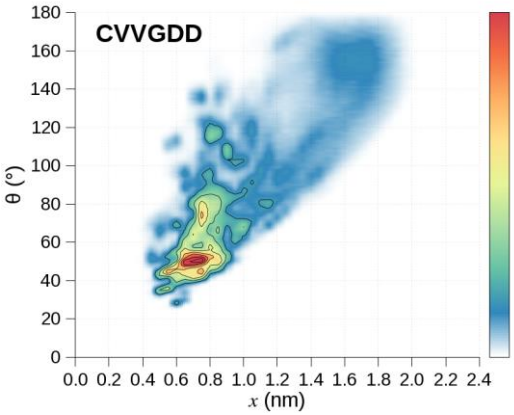
CVVGDD
θ (°)
x (nm)

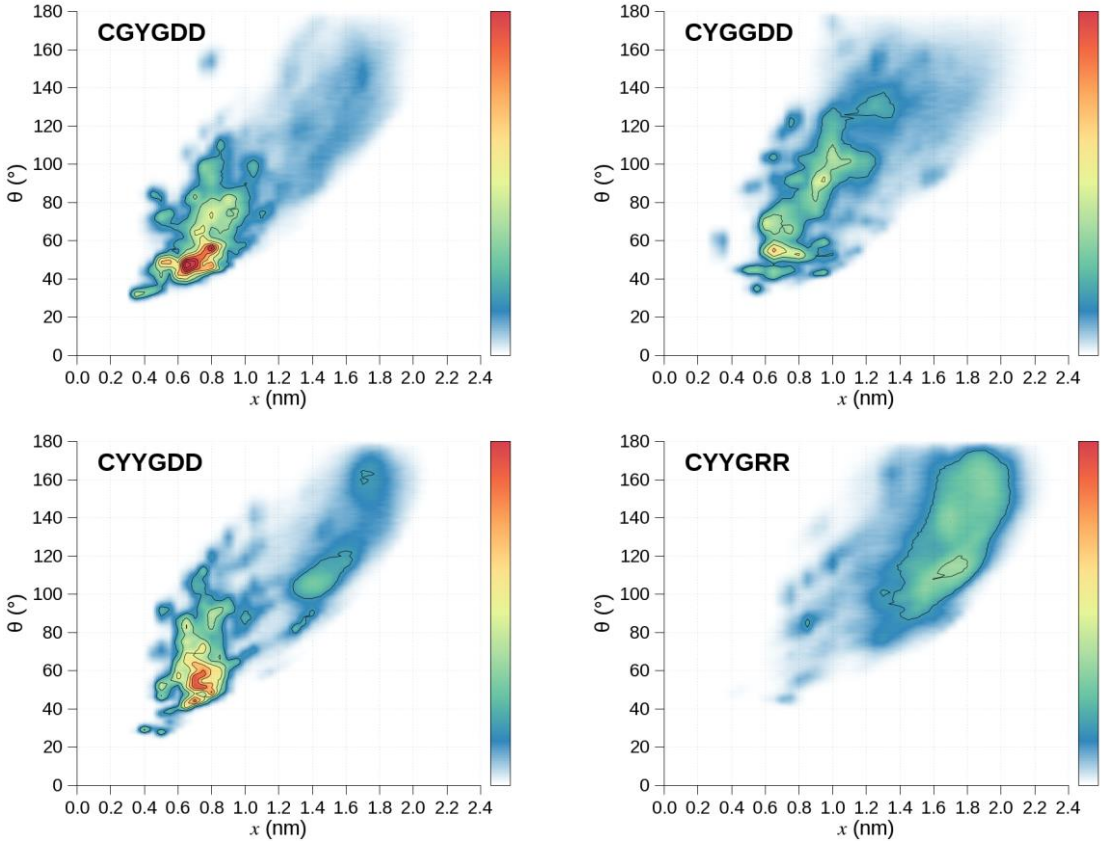

Figure S9. Density maps of peptide backbone angles formed throughout the MD simulations as a function of C-terminal to $AuS_{nearest}$ distances. Angle θ is measured between backbone alpha carbon atoms 1, 3 and 6 ($C\alpha_1$–$C\alpha_3$–$C\alpha_6$, where numbering starts from the N-terminus) and peptide C-terminal locations are taken as $C\alpha_6$ atom positions. Peptide conformations that are frequently and rarely visited are colored red/orange and white/blue, respectively.

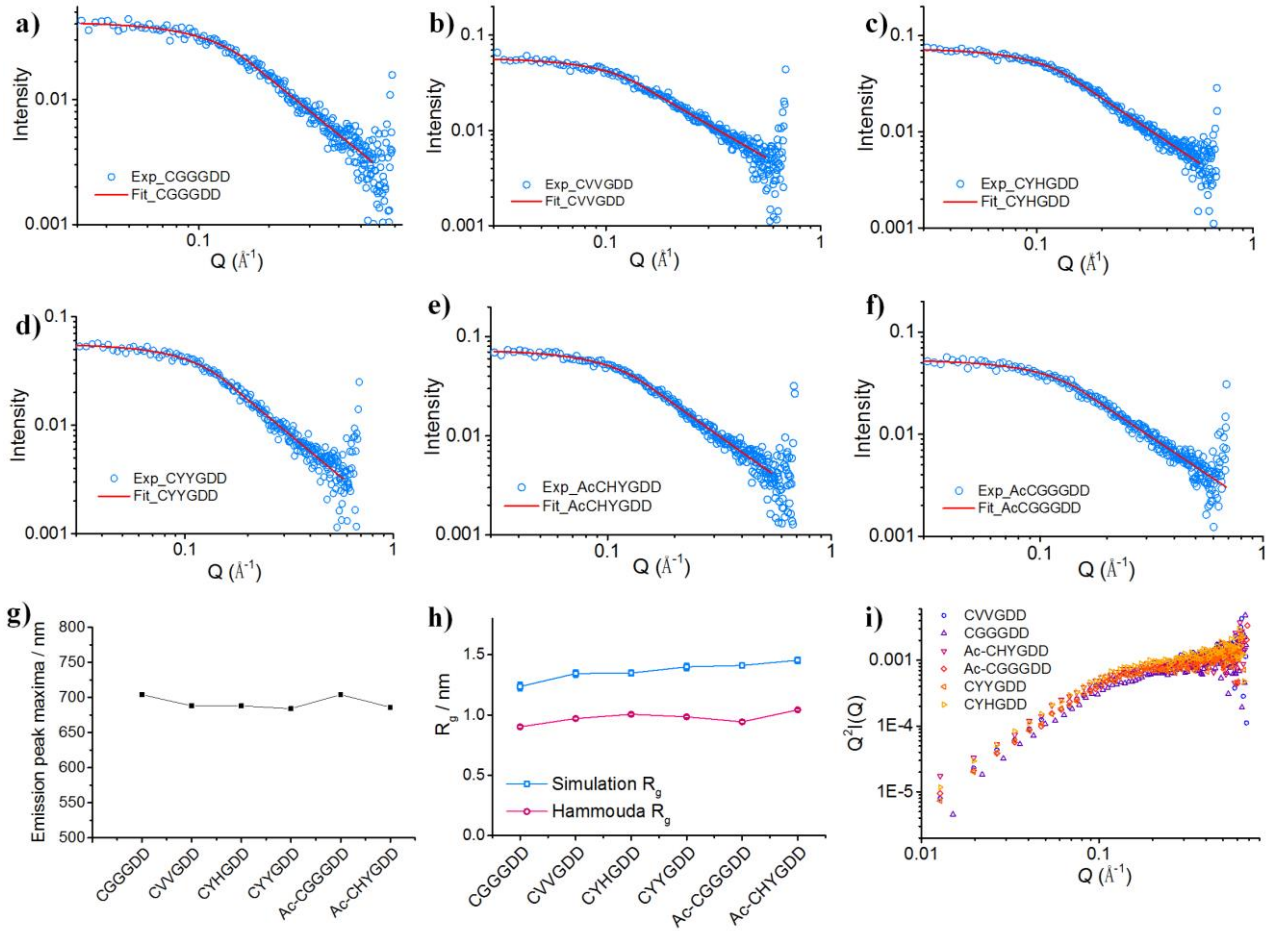

j)

Sequence	Scattering				Simulation R_g
	R_g / nm	R_g(Er) / nm	*P*	*P*(Er)	/ nm
CGGGDD	0.90	±0.01	1.50	±0.03	1.24
CVVGDD	0.97	±0.01	1.30	±0.02	1.34
CYHGDD	1.01	±0.01	1.50	±0.02	1.35
CYYGDD	0.99	±0.01	1.59	±0.02	1.40
Ac-CGGGDD	0.94	±0.01	1.45	±0.02	1.41
Ac-CHYGDD	1.04	±0.01	1.60	±0.02	1.45

Figure S10. (a-f) Plots of scattered X-ray intensity with *Q* (blue) as well as Hammouda's Guinier-Porod model simulation fits (red traces). (g) Plot of emission peak maxima as a function of peptide sequence (Figure S1) showing the minimal variation in peak position indicative of minimal variation in the Au core size. (h) Plot of the value of scattering R_g obtained for MD simulations (blue) and from the Hammouda model fits to the scattering data (pink) as a function of peptide sequence. (i) Kratky plots of scattered intensity highlighting the plateau formation of these systems which indicates flexible, extended peptide configurations. (j) Tabulated fit data for R_g and the Porod exponent *P* along with the MD simulation scattering R_g values obtained using Crysol.

The scattering data were measured using a Ganesha 300XL SAXS apparatus from SAXLAB (Denmark). The incident wavelength was 1.54 Å and the position of the Dectris Pilatus 300 area detector and diameter of the collimating pinholes were adjusted to give four overlapping ranges of scattering vector (0.003-0.018, 0.007-0.25, 0.015-0.65, 0.7-2.8 $Å^{-1}$). The samples were sealed in 1.5 mm fused quartz capillary tubes (Capillary Tube Supplies Ltd, Bodmin) and the all the beam paths were evacuated. The sample scattering was regrouped to a 1D dataset of intensity *vs* scattering vector, *Q*, then corrected for transmission and thickness using SAXSGUI. The scattering from the capillary tubes was measured from an empty part and subtracted. The pure solvent data was treated in the same way and subtracted from the solution data before further analysis.

Data were analysed using the NIST SANS data reduction package in Igor Pro (Wavemetrics, OH) software.[22] The specific model used to fit the data was the Guinier-Porod model, developed by Hammouda,[23] which is a generalized empirical model for structures having Guinier and Porod components (**Figure S10a-f**). The structures were assumed to be globular, allowing a generalized power law and scattering radius of gyration (R_g) to be obtained from the experimental data. The R_g obtained using this method will be susceptible to variation in the electron dense Au core size, which will contribute significantly to the scattered X-ray intensity. The fluorescence emission maxima of the clusters is known to vary as a function of cluster size[24] and we have used this indicator (**Figure S10g**) to suggest that there is minimal variation in core size where the emission peak maxima remains within the range of 680 to 705 nm. Indeed, any variation in peak maxima position does not follow the trend of increasing core size with increasing sequence hydrophobicity suggesting that the R_g values obtained in SAXS measurements and fitting relate to the contribution of the peptide shell. **Figure S10h** highlights the tendency for the SAXS derived R_g values to follow the same trend as the scattering R_g obtained for MD simulation trajectories (generated in Crysol for multiple trajectory frames and averaged) where an increase in sequence hydrophobicity tends to relate to an increase in R_g. However, for a fixed number of peptides per cluster, the role of scattering length density of the shells will be linked to the variation in shell thickness. In such a case the mixing ratio of peptide to solvent will vary and influence the R_g obtained experimentally and the presence of a complex interface between the electron dense gold core and organic shell may explain why the experimental R_g values tend to be lower than the generated MD simulation values.

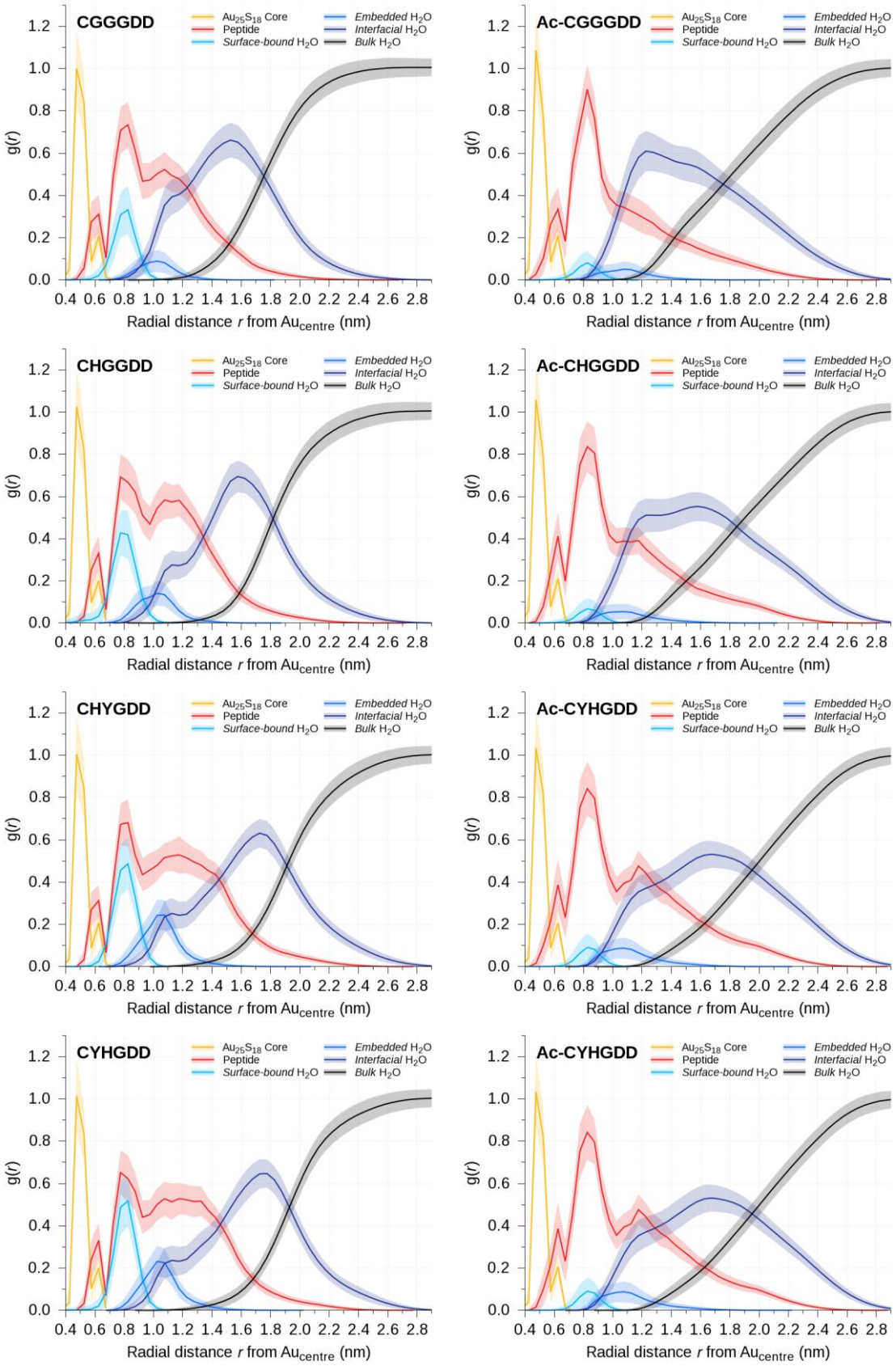
CGGGDD
Ac-CGGGDD
CHGGDD
Ac-CHGGDD
CHYGDD
Ac-CYHGDD
CYHGDD
Ac-CYHGDD
Au25S18 Core
Peptide
Surface-bound H2O
Embedded H2O
Interfacial H2O
Bulk H2O
g(r)
Radial distance r from Aucentre (nm)

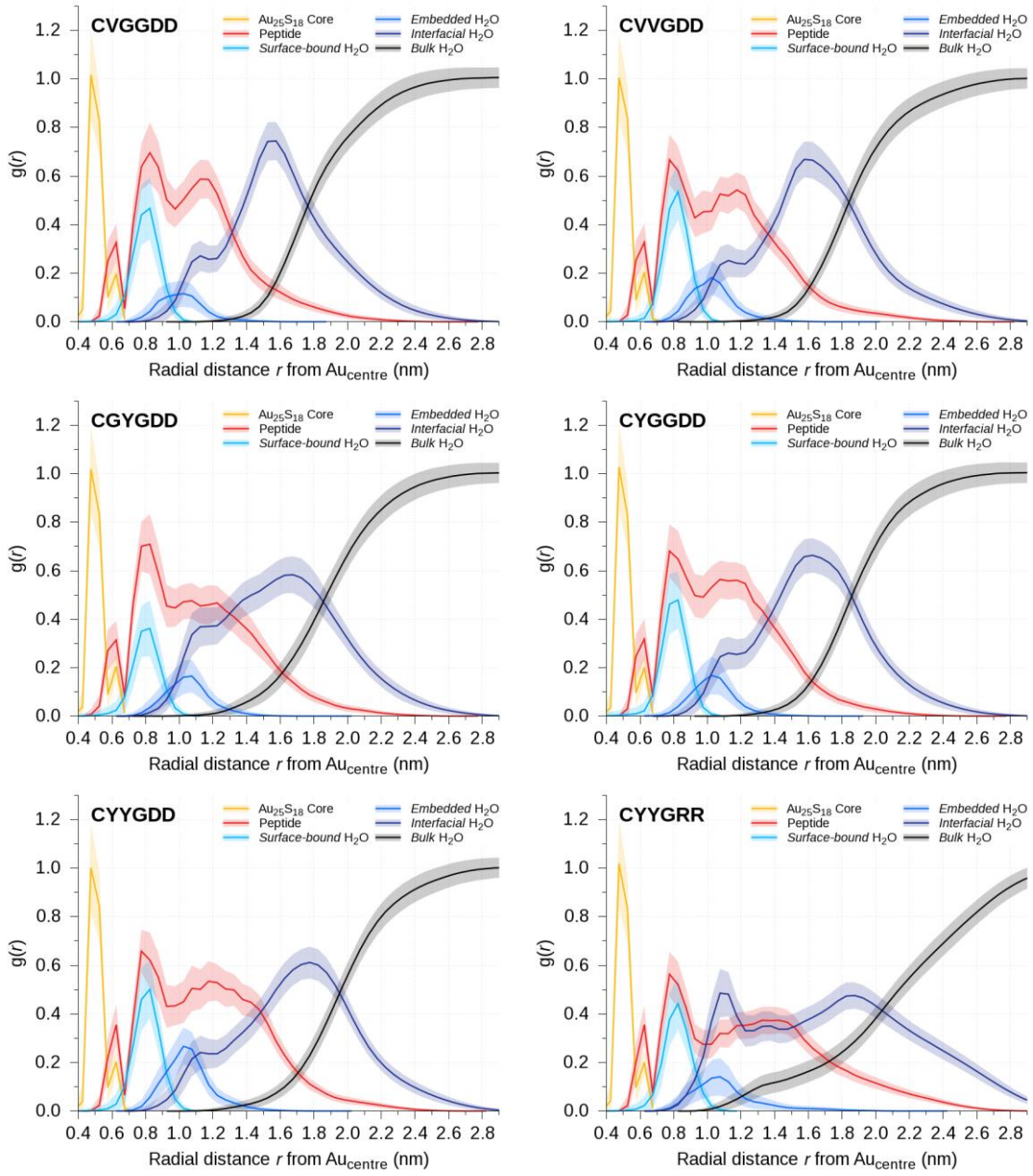

Figure S11. Radial distribution functions (RDF) of selected complex components relative to the central gold atom (Au_{center}) of the $Au_{25}(SP)_{18}$ to highlight water structuring between the different peptide sequences. $g(r)$ has been normalized by volume in each radial shell (dr = 0.05 nm) by the density of "bulk" water far from the AuNCs ($\rho_{bulk\text{-}water}$ = 0.100573). Explicitly, $g(r) = (N_{atoms}$ in V_{shell} / V_{shell}) / ($\rho_{bulk\text{-}water}$) = $[N_{(r+dr)} - N_r]$ / $[(4\pi/3)((r+dr)^3 - r^3)(\rho_{bulk\text{-}water})]$. Note that standard deviation is shown as the shaded region around each line.

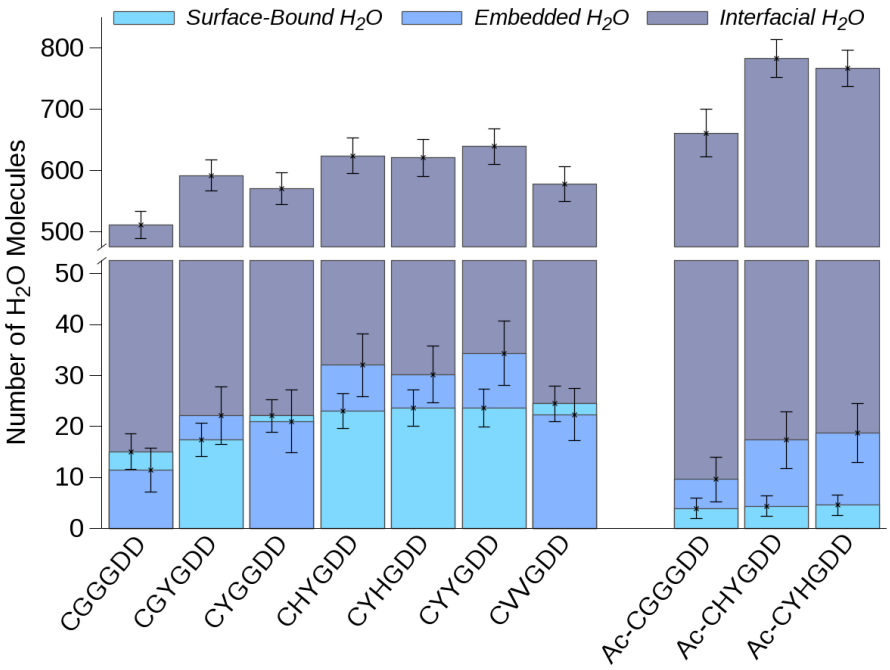

Figure S12. Superimposed histograms of the average number of H_2O molecules that are internalized (*surface-bound* and *embedded*) and present at the peptide–solvent hydration layer (*interfacial*) of each simulated $Au_{25}(SP)_{18}$ system. Error bars represent standard deviation.

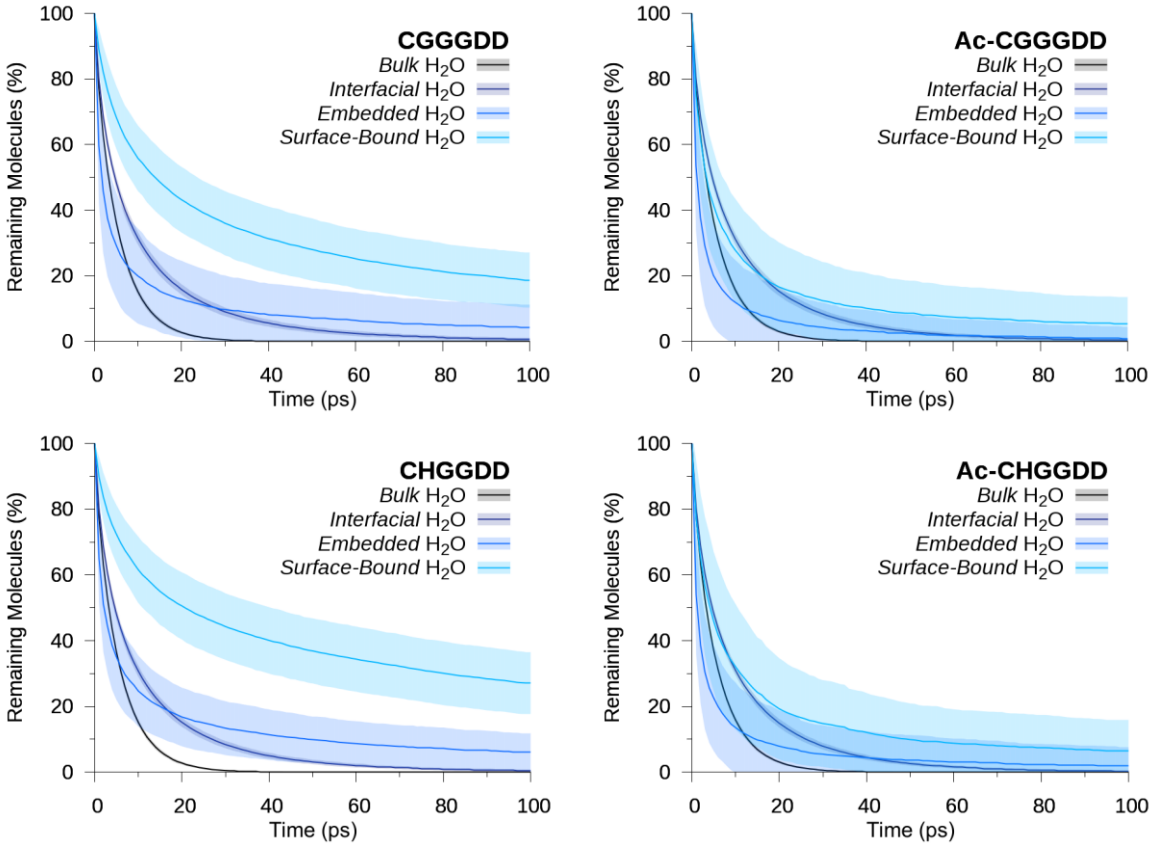

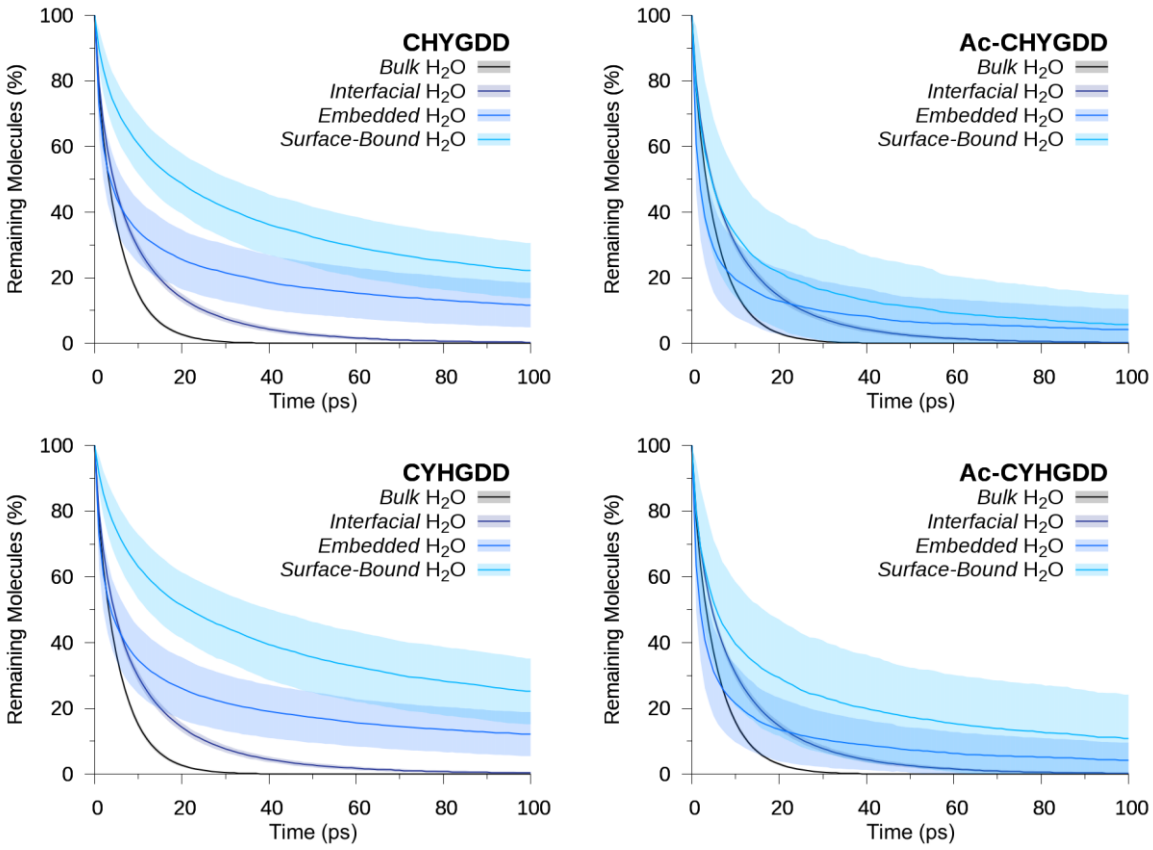

Figure S13. Water decay profiles (*bulk*, *interfacial*, *embedded*, or *surface-bound*) showing how internalized water has a much shorter retention time for acetylated $Au_{25}(SP)_{18}$ systems. Atom indices are monitored for each water selection (e.g. *bulk*, *interfacial*¸ etc.) in blocks of 100 ps at a frequency of 2 ps. At t = 0 ps, an initial selection of water atoms is made based on a distance criteria, then a count is maintained for molecules that consecutively remain in the selection over the 100 ps. To avoid correlated data, every 2nd trajectory block of 100 ps is not analyzed. At the end of data collection, all decays for a given system are averaged and presented with their standard deviation (shaded region). *Bulk* water profiles are obtained by using a 0.6 nm radial shell from *interfacial* water.

Table S3. Average bond distances in angstroms for the PBE/DNP optimized clusters with $–NH_2$, $–NH_3^+$, and $–COCH_3$ N-termini.

Bond type*	Experimental[a]	$–NH_2$	$–NH_3^+$	$–COCH_3$
$Au_{center}–Au_{shell}$ (12)	2.793 ± 0.006	2.787 ± 0.033	2.789 ± 0.030	2.789 ± 0.037
$Au_{shell}–Au_{shell}$ (30)	2.94 ± 0.09	2.935 ± 0.149	2.939 ± 0.156	2.938 ± 0.157
$Au_{shell}–S_{terminal}$ (12)	2.372 ± 0.020	2.369 ± 0.017	2.373 ± 0.019	2.370 ± 0.016
$Au_{staple}–S_{terminal}$ (12)	2.301 ± 0.008	2.290 ± 0.006	2.290 ± 0.004	2.290 ± 0.009
$Au_{staple}–S_{central}$ (12)	2.299 ± 0.013	2.294 ± 0.005	2.291 ± 0.005	2.294 ± 0.005

*Atom notation is taken from Weerawardene et. al [25] and Vanzan et. al [26] and number of bonds is given in parentheses.

[a] See reference [3]

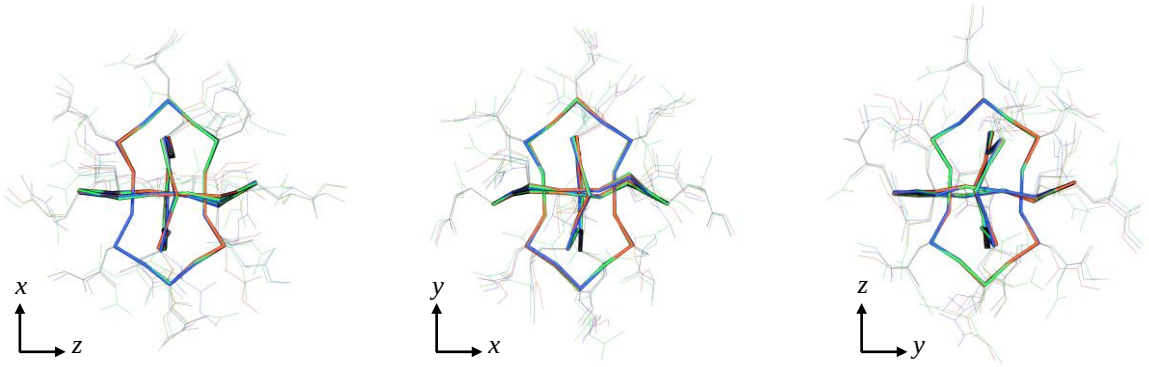

Figure S14. Overlay of the QM optimized $Au_{25}Cys_{18}$ structures, where cysteine N-termination is deprotonated amine ($–NH_2$, red), amide ($–NH_3^+$, blue), and acetyl ($–COCH_3$, green). The Au_{25} RMSD is ~0.1 Å between the three systems.

Moment of Inertia Tensor to Determine Nanocluster Size and Shape

The best fitting ellipsoid for each $Au_{25}(SP)_{18}$ is found using the moment of inertia tensor **I**, defined as:

$$\boldsymbol{I} = \begin{bmatrix} I_{xx} & I_{xy} & I_{xz} \\ I_{yx} & I_{yy} & I_{yz} \\ I_{zx} & I_{zy} & I_{zz} \end{bmatrix} = \sum_{i=1} m_i \begin{bmatrix} (y_i^2 + z_i^2) & -x_i y_i & -x_i z_i \\ -y_i x_i & (x_i^2 + z_i^2) & -y_i z_i \\ -z_i x_i & -z_i y_i & (x_i^2 + y_i^2) \end{bmatrix}$$

where m_i is the mass particle i at position (x_i,y_i,z_i) from the axis of rotation. The eigenvalues of the tensor are the principal moments of inertia $\tilde{I}_1$, $\tilde{I}_2$ and $\tilde{I}_3$ which can be obtained by the diagonalised tensor ($\tilde{\boldsymbol{I}}$):

$$\tilde{\boldsymbol{I}} = \begin{bmatrix} \tilde{I}_1 & 0 & 0 \\ 0 & \tilde{I}_2 & 0 \\ 0 & 0 & \tilde{I}_3 \end{bmatrix}$$

For an ellipsoid, the eigenvalues are:

$$\tilde{I}_1 = \frac{M}{5}(b^2 + c^2), \qquad \tilde{I}_2 = \frac{M}{5}(a^2 + c^2), \qquad \tilde{I}_3 = \frac{M}{5}(a^2 + b^2)$$

where M is the total mass and a, b and c are the major, intermediate and minor semi-axes lengths of the ellipsoid (i.e. $Au_{25}(SP)_{18}$, inset of **Figure S15**). AuNC volume is then calculated using $V = 4/3\pi abc$.

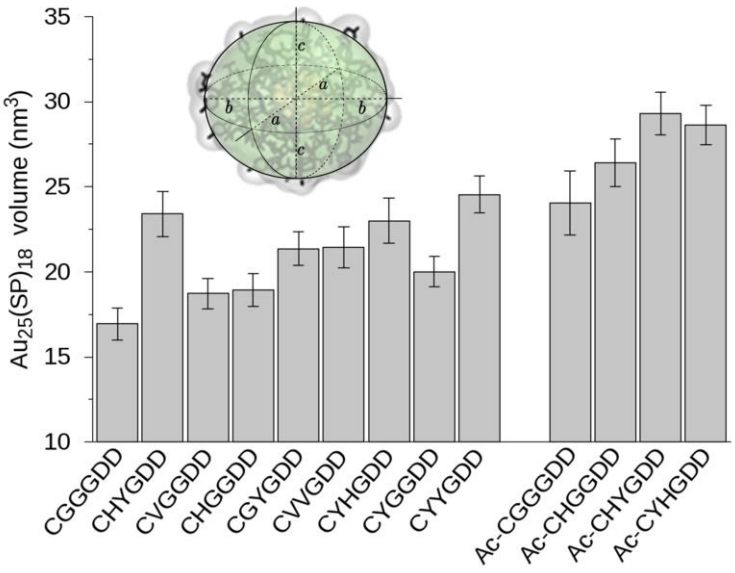

Figure S15. MD obtained average $Au_{25}(SP)_{18}$ volumes. The inset shows an example structure and the corresponding volume "ellipsoid" (green) displaying the major, intermediate and minor axes of the $Au_{25}(SP)_{18}$.

References

1. Negishi, Y.; Nobusada, K.; Tsukuda, T., *J. Am. Chem. Soc.* **2005,** *127*, 5261-5270.
2. Ghosh, A.; Udayabhaskararao, T.; Pradeep, T., *J. Phys. Chem. Lett.* **2012,** *3*, 1997-2002.
3. Dainese, T.; Antonello, S.; Gascón, J. A.; Pan, F.; Perera, N. V.; Ruzzi, M.; Venzo, A.; Zoleo, A.; Rissanen, K.; Maran, F., *ACS Nano* **2014,** *8*, 3904-3912.
4. Hess, B.; Kutzner, C.; van der Spoel, D.; Lindahl, E., *J. Chem. Theory Comput.* **2008,** *4*, 435-447.
5. Lindorff-Larsen, K.; Piana, S.; Palmo, K.; Maragakis, P.; Klepeis, J. L.; Dror, R. O.; Shaw, D. E., *Proteins: Struct., Funct., Bioinf.* **2010,** *78*, 1950-1958.
6. Jorgensen, W. L.; Chandrasekhar, J.; Madura, J. D.; Impey, R. W.; Klein, M. L., *J. Chem. Phys.* **1983,** *79*, 926-935.
7. Banerjee, S.; Montgomery, J. A., Jr.; Gascón, J. A., *J. Mater. Sci.* **2012,** *47*, 7686-7692.
8. Frisch, M. J.; Trucks, G. W.; Schlegel, H. B.; Scuseria, G. E.; Robb, M. A.; Cheeseman, J. R.; Scalmani, G.; Barone, V.; Mennucci, B.; Petersson, G. A.; Nakatsuji, H.; Caricato, M.; Li, X.; Hratchian, H. P.; Izmaylov, A. F.; Bloino, J.; Zheng, G.; Sonnenberg, J. L.; Hada, M.; Ehara, M.; Toyota, K.; Fukuda, R.; Hasegawa, J.; Ishida, M.; Nakajima, T.; Honda, Y.; Kitao, O.; Nakai, H.; Vreven, T.; Montgomery, J. A., Jr.; Peralta, J. E.; Ogliaro, F.; Bearpark, M. J.; Heyd, J.; Brothers, E. N.; Kudin, K. N.; Staroverov, V. N.; Keith, T.; Kobayashi, R.; Normand, J.; Raghavachari, K.; Rendell, A. P.; Burant, J. C.; Iyengar, S. S.; Tomasi, J.; Cossi, M.; Rega, N.; Millam, N. J.; Klene, M.; Knox, J. E.; Cross, J. B.; Bakken, V.; Adamo, C.; Jaramillo, J.; Gomperts, R.; Stratmann, R. E.; Yazyev, O.; Austin, A. J.; Cammi, R.; Pomelli, C.; Ochterski, J. W.; Martin, R. L.; Morokuma, K.; Zakrzewski, V. G.; Voth, G. A.; Salvador, P.; Dannenberg, J. J.; Dapprich, S.; Daniels, A. D.; Farkas, Ö.; Foresman, J. B.; Ortiz, J. V.; Cioslowski, J.; Fox, D. J.; Gaussian, Inc.: Wallingford, CT, USA, 2010.
9. Torda, A. E.; Scheek, R. M.; van Gunsteren, W. F., *Chem. Phys. Lett.* **1989,** *157*, 289-294.
10. Berendsen, H. J. C.; Postma, J. P. M.; van Gunsteren, W. F.; Di Nola, A.; Haak, J. R., *J. Chem. Phys.* **1984,** *81*, 3684-3690.
11. Hoover, W. G., *Phys. Rev. A: Gen. Phys.* **1985,** *31*, 1695-1697.
12. Nosé, S., *Mol. Phys.* **1984,** *52*, 255-268.
13. Parrinello, M.; Rahman, A., *J. Appl. Phys.* **1981,** *52*, 7182-7190.
14. Humphrey, W.; Dalke, A.; Schulten, K., *J. Mol. Graph.* **1996,** *14*, 33-38.
15. Kang, E.-H.; Mansfield, M. L.; Douglas, J. F., *Phys. Rev. E: Stat., Nonlinear, Soft Matter Phys.* **2004,** *69*, 031918.
16. Fihey, A.; Maurel, F.; Perrier, A., *J. Phys. Chem. C* **2014,** *118*, 4444-4453.
17. Delley, B., *The Journal of Chemical Physics* **2000,** *113*, 7756-7764.
18. Perdew, J. P.; Burke, K.; Ernzerhof, M., *Phys. Rev. Lett.* **1996,** *77*, 3865-3868.
19. Delley, B., *The Journal of Physical Chemistry A* **2006,** *110*, 13632-13639.
20. Delley, B., *Mol. Simul.* **2006,** *32*, 117-123.
21. Tomasi, J.; Mennucci, B.; Cammi, R., *Chem. Rev.* **2005,** *105*, 2999-3093.
22. Kline, S., *J. Appl. Crystallogr.* **2006,** *39*, 895-900.
23. Hammouda, B., *J. Appl. Crystallogr.* **2010,** *43*, 716-719.
24. Mishra, D.; Aldeek, F.; Lochner, E.; Palui, G.; Zeng, B.; Mackowski, S.; Mattoussi, H., *Langmuir* **2016,** *32*, 6445-6458.
25. Weerawardene, K. L. D. M.; Aikens, C. M., *J. Am. Chem. Soc.* **2016,** *138*, 11202-11210.
26. Vanzan, M.; Corni, S., *The Journal of Physical Chemistry A* **2018,** *122*, 6864-6872.